ADVANCED MATERIALS
www.advmat.de

Beyond Gold: Spin-Coated Ti_3C_2-Based MXene Photodetectors

*Kiana Montazeri, Marc Currie, Louisiane Verger, Pouya Dianat, Michel W. Barsoum, and Bahram Nabet**

2D transition metal carbides, known as MXenes, are transparent when the samples are thin enough. They are also excellent electrical conductors with metal-like carrier concentrations. Herein, these characteristics are exploited to replace gold (Au) in GaAs photodetectors. By simply spin-coating transparent Ti_3C_2-based MXene electrodes from aqueous suspensions onto GaAs patterned with a photoresist and lifted off with acetone, photodetectors that outperform more standard Au electrodes are fabricated. Both the Au- and MXene-based devices show rectifying contacts with comparable Schottky barrier heights and internal electric fields. The latter, however, exhibit significantly higher responsivities and quantum efficiencies, with similar dark currents, hence showing better dynamic range and detectivity, and similar sub-nanosecond response speeds compared to the Au-based devices. The simple fabrication process is readily integratable into microelectronic, photonic-integrated circuits and silicon photonics processes, with a wide range of applications from optical sensing to light detection and ranging and telecommunications.

Photodetectors have a wide range of applications and are presently in great demand due to the explosion in information, data transport, and processing needs, that is facilitated by fiber optics tele/data communications. In particular, high bandwidth is essential for data center operations supporting applications such as Internet of things (IoT), autonomous vehicles, artificial intelligence, and virtual reality among other Internet demands. The need for high-speed, high-responsivity detection is traditionally met by p-type–intrinsic–n–type (PIN) photodiodes,[1] avalanche photodiodes (APD),[2] metal–semiconductor–metal (MSM),[3,4] or metal–graphene–metal[5–7] photodetectors.

Of these, top-illuminated, MSM devices are planar, relatively easy to fabricate, and are more readily integratable with field effect transistor (FET) technology as they exploit the same Schottky contacts used for the FET gate, and do not require the p and n doping of the bipolar technology. MSM photodetectors consist of two Schottky contacts typically fabricated as interdigital electrodes on top of a semiconductor.[3,4] These metallic contacts—typically Ti/Pt/Au[8] for GaAs and other III–V semiconductors—are produced by patterning a substrate by conventional photolithography, and subsequently depositing a metal under vacuum by either evaporation or sputtering, followed by either lift-off or etching. Light is absorbed between the contacts and the optically generated carriers are swept into them by an externally applied electric field that enhances the internal field of the rectifying Schottky contacts.[9,10]

MSM photodetectors, however, have higher dark currents, I_{dark}, hence higher noise, compared to PINs and APDs, although several techniques exist to reduce I_{dark} by, e.g., increasing the rectifying Schottky barrier heights of the metal–semiconductor interfaces using a wider bandgap semiconductor such as AlGaAs,[11] establishing a reduced dimensional final density of states in the semiconductor,[12] and producing confined carrier gases which repel the injected electrons from the metal.[13] For all these devices, high responsivity requires larger absorption areas.[14] However, increasing a device's surface area limits its bandwidth both by increasing the RC time constants, and transit times of the optically generated carriers to the collection electrodes.[15] A tradeoff therefore needs to be engineered depending on application.

The MXene family is one of the latest additions to the world of 2D materials. MXenes are 2D transition metal carbides or carbonitrides, discovered in 2011[16] and currently number around 30, with new ones discovered on a regular basis. MXenes are typically produced by selective etching the A-layers from the $M_{n+1}AX_n$ phases.[17] The latter are layered, machinable ternary carbides and nitrides, where M is an early

K. Montazeri, Dr. P. Dianat, Prof. B. Nabet
Electrical and Computer Engineering Department
Drexel University
Philadelphia, PA 19104, USA
E-mail: nabetb@drexel.edu

Dr. M. Currie
Optical Sciences Division
Naval Research Laboratory
Washington, DC 20375, USA

Dr. L. Verger, Prof. M. W. Barsoum
Materials Science and Engineering Department
Drexel University
Philadelphia, PA 19104, USA

Dr. P. Dianat
Nanograss Solar LLC
1407 Bethlehem Pike, Suite 303, Flourtown, PA 19031, USA

The ORCID identification number(s) for the author(s) of this article can be found under https://doi.org/10.1002/adma.201903271.

DOI: 10.1002/adma.201903271

Printed by [Drexel University Drexel Unive - 144.118.077.011 - /doi/epdf/10.1002/adma.201903271] at [28/05/2020].

 © 2019 WILEY-VCH Verlag GmbH & Co. KGaA, Weinheim

transition metal, A is an A-group element, and X is C and/or N and n = 1 to 3. Upon etching, the A-layers, mostly Al, are replaced by various surface terminations, mostly —O, —OH, and/or —F,[18] although recent studies show that novel terminations such as Cl[19] can also be engineered.

Interest in MXenes has exploded recently for a number of reasons, chief among them is that they are hydrophilic and yet quite conductive. Another reason is the ease by which large quantities of stable aqueous colloidal suspensions are produced. A number of excellent review articles exist on these materials.[20–25] To date, MXenes have been used in numerous applications, achieving, in many cases, record values. MXenes have been used as electrodes in batteries and electrochemical capacitors,[26] textile supercapacitors,[27,28] photodetectors,[29] electrical contacts such as Schottky electrodes,[30] or ohmic contacts with modified MXene chemistries,[31] and spayed-on antennas.[32] Since transparent contacts are widely used for touch sensitive screens,[33] solar cells,[34] and organic light emitting diodes (OLED),[35] MXenes could also be materials of choice for these applications.

Using MXene transparent contacts offers an obvious advantage that mitigates the aforementioned tradeoff between carrier transit distance and responsivity, should they maintain, as shown below, other important attributes of Schottky metal–semiconductor contacts such as large barrier heights, built-in potentials, and large internal electric fields.[15] As just noted, if thin enough, MXene films are both conductive and transparent.[36–38] Here, we deposit transparent, metallic $Ti_3C_2T_z$-based contacts on gallium arsenide (GaAs), substrates to produce MXene–semiconducting–MXene, henceforth referred to as MX–S–MX, photodetecting devices. The purpose of this work is to quantify the optoelectronic characteristics of MX–S–MX devices and compare them to conventional MSM devices with Ti/Au Schottky contacts. In what follows, we produce thin MXene films and characterize their optical properties. In order to construct a device, however, it is necessary to pattern the electrodes. MXene patterning has previously been carried out using laser printers,[39] or microcontact printing techniques.[40] The resulting feature sizes—in the hundreds of micrometers range—are too large for our purpose. Microintaglio printing has been used for patterning other types of 2D materials,[41] carried out in vacuum chambers. Here, we show that much finer patterning, limited by our photolithography, is possible, where the MXene films are spin-coated on GaAs substrates and lifted off by simple immersion in acetone. Schematics of the fabrication processes and resulting devices together with energy band diagrams are shown in **Figure 1**. The process used, shown schematically in Figure 1, is carried out at room temperature in ambient air, and resulted in device feature sizes of the order of 2 µm, although the devices studied here have larger separations between contacts. The results reported below confirm that this inexpensive, simple, scalable process results in photodetectors

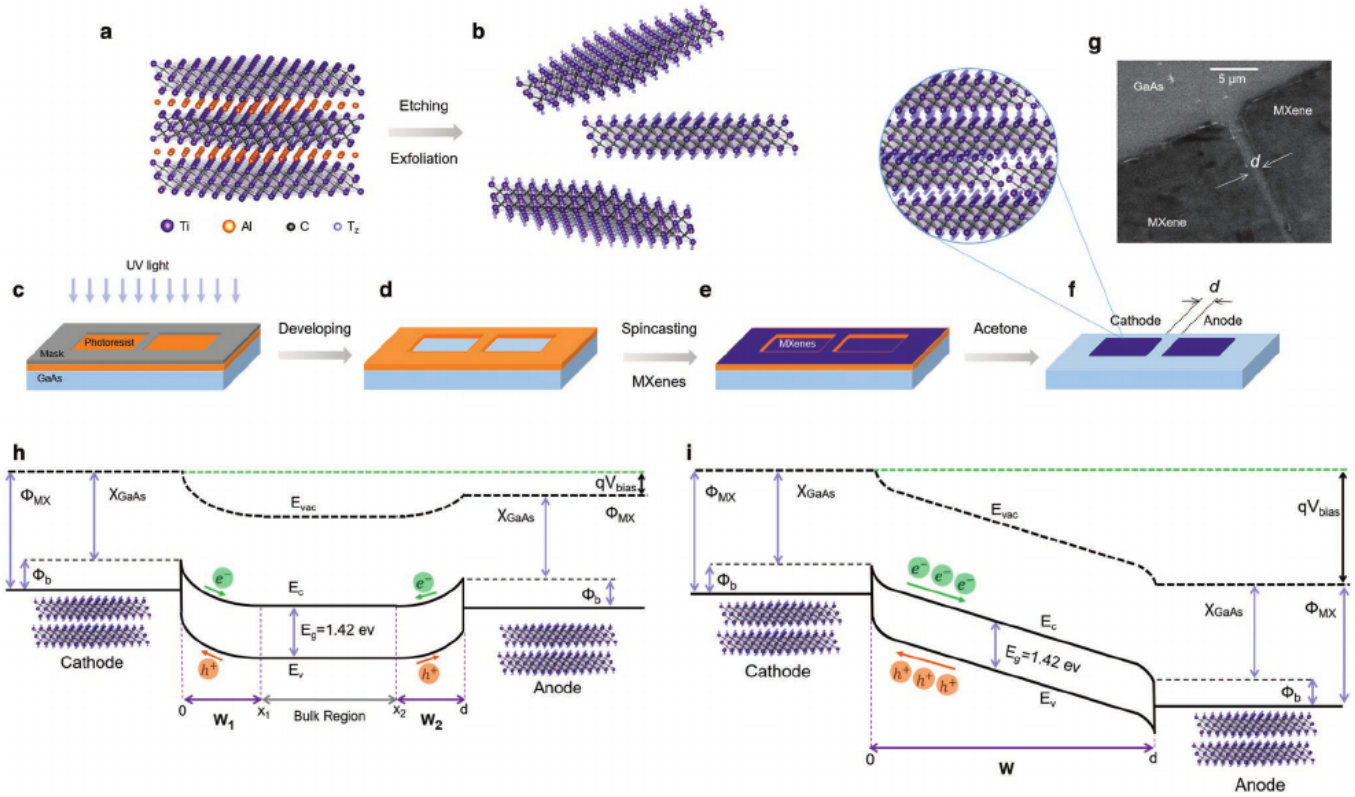

Figure 1. Fabrication process and energy band diagrams for MXene–GaAs–MXene (MX–S–MX) photodetector devices. a,b) Preparation of MXene colloidal suspension. In (c) and (d), conventional photolithography is performed resulting in exposed areas for contact deposition. e) MXene aqueous colloidal suspension is spin-coated, and f) lifted off by immersion in acetone. g) SEM of the final device showing cathode–anode separation gap. h) Sketch of the energy band diagram of device under moderate bias—showing the Schottky contacts at cathode and anode, the barrier height, built-in voltage, internal field, and depletion regions. i) Same as (h), but under high biasing voltage resulting in flat-band conditions.

Printed by [Drexel University Drexel Unive - 144.118.077.011 - /doi/epdf/10.1002/adma.201903271] at [28/05/2020].

© 2019 WILEY-VCH Verlag GmbH & Co. KGaA, Weinheim

that were as good as and, in most attributes, better than those fabricated with Ti/Au electrodes.

The MXene chosen for this work is $Ti_3C_2T_z$ because it is by far the most studied and thus best understood. To make our devices, first the Ti_3AlC_2 MAX phase (Figure 1a) was etched and delaminated (Figure 1b). The electrode pattern was then formed using photoresist and contact lithography on the GaAs substrate (Figure 1c) and developed (Figure 1d). The MXene colloidal suspension was then spin cast on the substrate (Figure 1e). Lastly, the photoresist was removed by immersing the device in acetone (Figure 1f) leaving two MXene pads. Spacings as narrow as 2 µm were obtained. The sharpness of the edges and corners is noteworthy, indicating that the resolution of this method is limited by lithography; our results are orders of magnitude better than prior work.[39,40] Details of the fabrication methods and experimental techniques can be found in the Experimental Section and Section S1 in the Supporting Information. The energy band diagram of our MX–S–MX device is shown in Figure 1h under moderate bias, and under large external bias in Figure 1i.

Before photodetector device fabrication, a thin $Ti_3C_2T_z$ film was deposited on a silica substrate. Details of the film preparation by spin casting is provided in Section S1 in the Supporting Information. **Figure 2** shows the measured transmittance and reflectance of a $Ti_3C_2T_z$ film of thickness ≈19.2 nm, indicated as "thin," which was used for device fabrication. The absorptance spectrum, absorptance = 1 − (reflectance + transmittance), is calculated in Figure 2c, the inset of which shows that half of the silica samples were covered and provide the baseline spectra that is shown in these figures. The wide absorption spectra, from 350 to 2200 nm, of these films are notable, with the interesting attribute of high absorptance in the UV range.

Figure 1g shows typical scanning electron microscopy (SEM) images of two Ti_3C_2-based pads separated by a gap of ≈2 µm. The results reported below confirmed that this inexpensive, simple, scalable process resulted in photodetectors that were as good as and, in most figures of merit (FOM), better than those fabricated with Ti/Au electrodes. This is notable given that—apart from the mask aligner—nothing more sophisticated than a tabletop spin-coater was needed. This ambient condition process can be readily integrated into microelectronic, photonic-integrated circuit (PIC), and silicon photonics (SiP) processes, with a wide spectrum of possible applications ranging from optical sensing to light detection and ranging (LiDAR), to optical tele/data communications.

To allow for side-by-side comparisons, Ti/Au–GaAs–Ti/Au MSM devices were fabricated using the same mask set and lithography technique as for the MX-based devices. In this case, electron-gun evaporation of, first a 5 nm Ti adhesion layer, followed by a 120 nm Au layer was used to deposit the electrodes. Pictures of the two devices are shown side by side in **Figure 3**a,e. Figure 3 compares the current–voltage (I–V) optical response of identical geometry devices—one MXene (left-hand column) and the other Au-based (right-hand column)—under dark and at wavelengths of 532, 780, and 830 nm as a function of bias. The λ of 532 and 780 nm were used to stress contact transparency; the 830 nm because it is used for high-speed, short-range optical tele/data communications applications.

Figure 3 shows that the MXene-based device has a dark current, I_{dark} of 0.6 nA at (533 nm) and 0.9 nA at (780 and 830 nm) for MX, which is comparable to 0.2 nA for Ti/Au MSM, and is remarkably low for such a large area device. In order to investigate the mechanisms of I_{dark} flow across the MXene-semiconductor junction devices with cathode–anode gaps of 5, 15, and 35 µm, respectively, were fabricated. Section S3 (Figure S1) in the Supporting Information shows that I_{dark} is independent of gap size, and relatively independent of the applied voltage. Had the contacts been ohmic, the current would have changed by a factor of 3 and 7, respectively, relative to the 5 µm gap of the device shown in Figure S1a in the Supporting Information. This means that a rectifying Schottky barrier exists at the MX–S interface, which dominates current transport. It follows that the energy band diagrams depicted in Figure 1h,i are applicable. This also implies band bending and the presence of an internal electric field at the contacts, which in turn affects the transport and collection of the optically generated carriers.

Besides having similar I_{dark}, hence noise, a remarkable five orders of magnitude change in photocurrent is observed at 8 V bias under illumination by 0.34 µW of optical power. A comparison of the photocurrent versus optical power is shown in **Figure 4** for λ = 532, 780, and 830 nm, at various biases. It is clearly observed that replacing Au with MXene substantially improves the optical response, particularly for λ = 830 nm where an enhancement by a factor of nearly 4 is observed at 8 V bias.

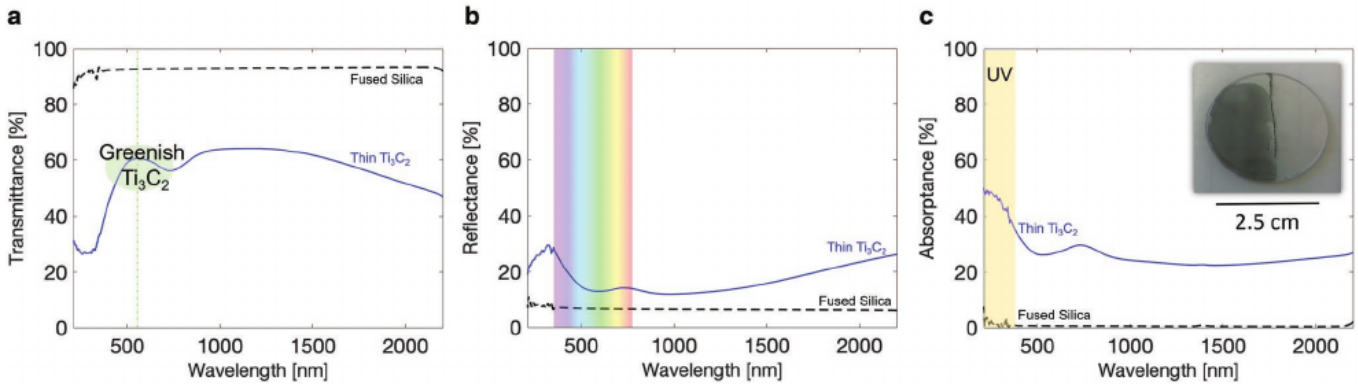

Figure 2. Optical properties of the Ti_3C_2 film with nominal thickness of 19.2 nm compared to the silica baseline. a) Measured transmission; and b) reflection spectra. c) Absorptance = 1 − (reflectance + transmittance). Inset in (c) shows a silica substrate half of which was covered and used for comparison. Wide spectral opacity and nearly 30% absorptance from 350–2200 nm in addition to high absorptance in UV range are notable.

Printed by [Drexel University Drexel Unive - 144.118.077.011 - /doi/epdf/10.1002/adma.201903271] at [28/05/2020].

 © 2019 WILEY-VCH Verlag GmbH & Co. KGaA, Weinheim

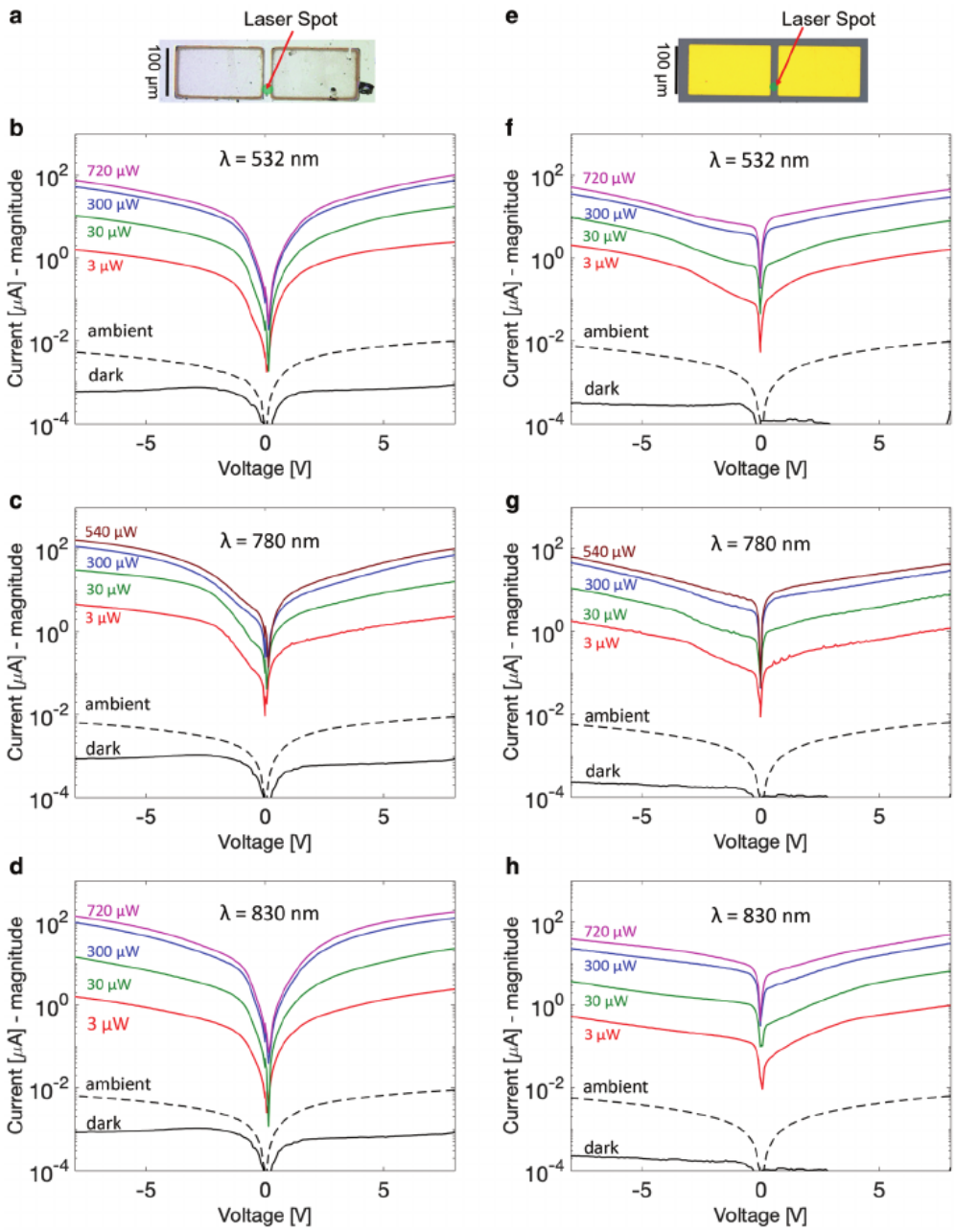

Figure 3. Comparison of current–voltage characteristics of MXene–GaAs–MXene (MX–S–MX) and conventional Ti/Au–GaAs–Ti/Au (MSM) photodetectors with gap spacing of 10 μm. a) Confocal microscopy image of the fabricated MX–S–MX photodetector with an overlay of the laser spot size, and e) the same but for MSM. b–d) Current–voltage responses of MX–S–MX to 532, 780, and 830 nm wavelength light, respectively. f–h) The same as (b)–(d), respectively, but for the MSM device.

Responsivity, defined as the ratio of photocurrent to incident optical power $R = \frac{I_{ph}}{P_{opt}}$ [mA W^{-1}] can be extracted. The results are listed in **Table 1**.

External quantum efficiency (QE), η is defined as the number of electrons circulating in the external circuitry per incident photon, and relates to responsivity by:[42] $\eta = \frac{1.24 \times R}{\lambda}$ (λ in μm), and is detailed in Section S4 (Figure S2) in the Supporting Information. That data is consistent with Figure 4 and Table 1. It shows that replacing Au by MXene in these devices substantially increases their responsivity and quantum efficiency for all wavelengths and at all bias levels. In fact, the 280 mA W^{-1} responsivity observed under 8 V bias at 830 nm meets the stringent needs of LiDAR applications,[43,44] is quite remarkable for this simple device and is better than the Ti/Au-device responsivity of ≈72 mA W^{-1} (see Table 1).

Responsivity (R), relates to detectivity $D^* = R/\sqrt{\frac{2q}{A} I_{dark}}$, and allows us to determine an important figure of merit, the noise equivalent power (NEP), which determines the minimum incident power, where the detector can distinguish a signal from the background noise level. NEP may be approximated as[45]

© 2019 WILEY-VCH Verlag GmbH & Co. KGaA, Weinheim

Printed by [Drexel University Drexel Unive - 144.118.077.011 - /doi/epdf/10.1002/adma.201903271] at [28/05/2020].

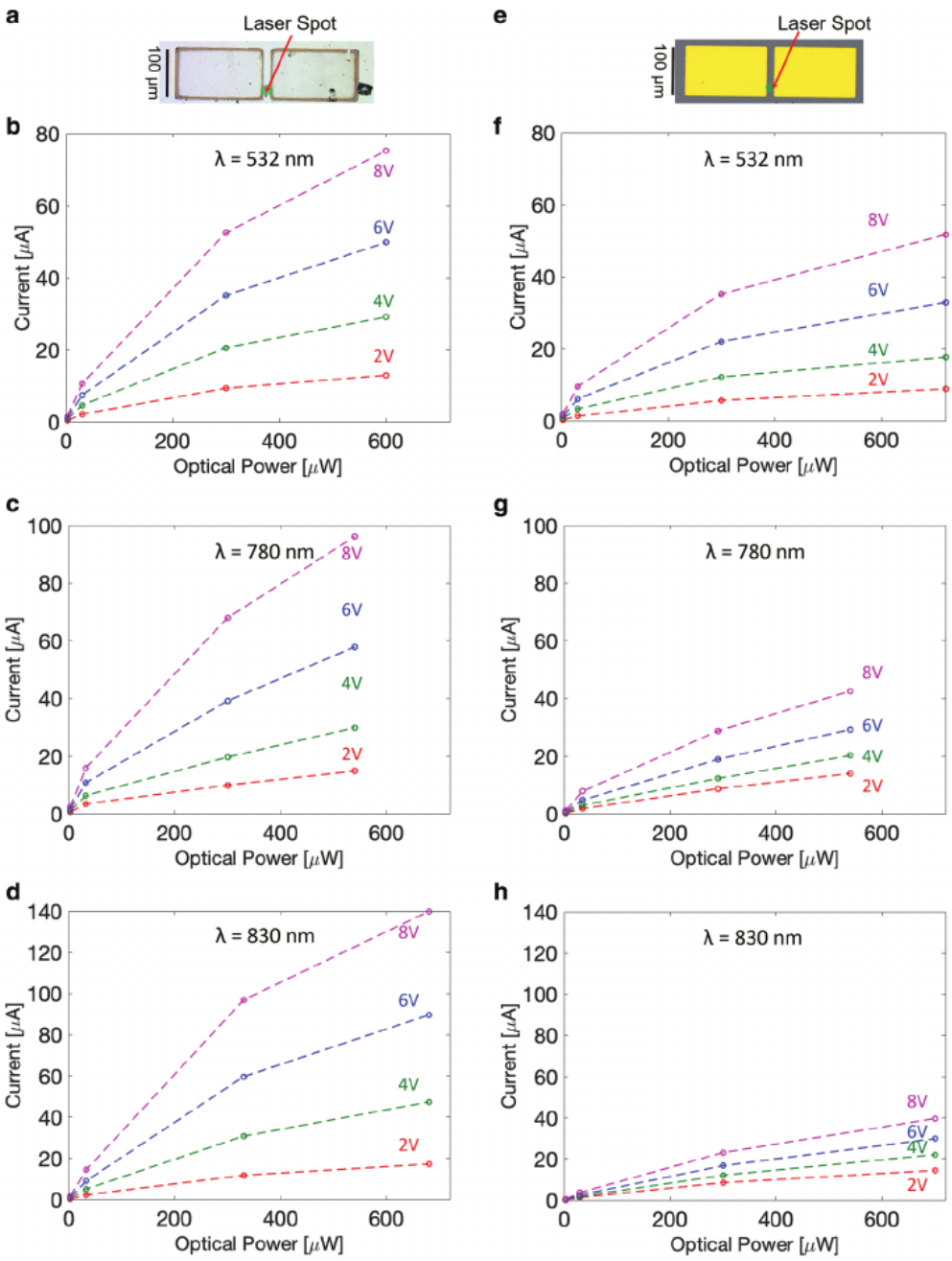

Figure 4. a–e) Comparison of MX–S–MX (a) (left column) and MSM (e) (right column) detectors' photocurrent under various optical intensities and at different biases and with gap spacing of 10 μm. Top row: b,f) response to $\lambda = 532$ nm incident light. Middle row: c,g) $\lambda = 780$ nm. Bottom row: d,h) $\lambda = 830$ nm. MX–S–MX detector outperforms the Ti/Au-based device with up to 300% more responsivity at all measured wavelengths, most significantly at λ = 830 nm.

$\mathrm{NEP} = \sqrt{(A \cdot \Delta f)}/D^*$, where Δf is the measurement bandwidth and A is the active area of the device taken to be the area of the laser spot in both cases.

Table 2 provides a comparison of the MXene- and Ti/Au-based devices on the basis of several FOMs, namely, R [mA W^{-1}], QE, D^* [Jones], NEP $\left[\frac{\mathrm{W}}{\sqrt{\mathrm{Hz}}}\right]$, and dynamic range (DR) [dB] defined as $10\log_{10}\frac{P_{\mathrm{in}}}{\mathrm{NEP}}$, where P_{in} is optical input power. Further insight into the large DR is provided in Figure 4 which shows photocurrent versus incident optical power at three wavelengths and several bias conditions, as well as Figure S2 in the Supporting Information which compares the external quantum efficiency of Au- and MXene-based devices at these wavelengths. On the basis of all these FOMs, the MXene-based device that is simply spun on a wafer and dipped in acetone, outperforms Ti/Au by a large margin, the most impressive of which, perhaps, is achieving nearly four times improvement in R at the desirable wavelength of 830 nm (Table 1). Considering these FOMs, the MX–S–MX devices

Printed by [Drexel University Drexel Unive - 144.118.077.011 - /doi/epdf/10.1002/adma.201903271] at [28/05/2020].

 © 2019 WILEY-VCH Verlag GmbH & Co. KGaA, Weinheim

Table 1. Responsivity [mA W^{-1}] at ≈300 μW input power.

Bias [V]	MXene–GaAs–MXene			Ti/Au MSM		
	532 nm	780 nm	830 nm	532 nm	780 nm	830 nm
2	27	24	32	16	26	27
4	59	50	86	33	36	38
6	103	106	170	59	55	53
8	155	195	278	95	82	72

have enhanced performance metrics compared to a number of 2D-based photodetector technologies currently in use.[46]

To emphasize the importance of electrode contact transparency, we illuminated a corner of our MXene-based device as shown in Section S4 (Figure S1d) in the Supporting Information. A change in photocurrent by a factor of ≈400 was obtained due to the transparency of the contacts, and does not have a counterpart in the Ti/Au MSM device. This provides a promising platform in cases where the light source is highly divergent, and is difficult to focus all the light power on an active region with narrow feature sizes. The transparency of the contacts as well as their increase in conductivity under illumination are potentially useful in applications such as neuronal recording,[47] particularly for optogenetics purposes.[48]

The devices' optoelectronic response was measured at four average optical powers (3, 30, 300, and 700 μW) with 8 V of bias applied through a bias-T. **Figure 5**a shows the MXene-based device's response, while Figure 5b is the pulse response of the Ti/Au device, which compare temporal responses at 300 μW optical power. Measured fall time and pulse width values are given on Figure 5 and reported for other optical powers in Section S5 (Figure S3) in the Supporting Information. Our MXene-based device exhibits a fast pulse width of 225 ps, which, although slower than Ti/Au's 78 ps, still corresponds to operation near the 3 GHz range, which meets many of present speed requirements and is orders of magnitude better than competing previous works in perovskite/MXene devices that reported an 18 ms time response.[49] Considering the large cathode–anode transit distance in present devices, optimization of device geometry should result in faster MXene-based devices.

As experimentally shown above, the MXene–GaAs contacts are rectifying (Schottky), hence I_{dark} of the MX–S–MX device is dominated by the properties of the reverse biased cathode, described by the Richardson and Dushman equation[50,51]

$$I_{\text{dark}} = A^{*}T^{2}A\exp\left(\frac{-q\phi_{\text{B}}}{K_{\text{B}}T}\right)\exp\left(\frac{q\Delta\phi_{\text{im}}}{K_{\text{B}}T}\right) \quad (1)$$

where ϕ_{B} is the Schottky barrier height, A^* is the Richardson constant, ϕ_{im} is the barrier lowering due to the image force, and other symbols have their usual meaning. Equation (1) shows the significance of the Schottky barrier height in determining the I_{dark} values. In the limiting case, that the semiconductor has no surface states, the barrier height is the difference of the metal work function (ϕ_{m}) and semiconductor electron affinity (χ_{s}):[52] $\phi_{\text{B}} = \phi_{\text{m}} - \chi_{\text{s}}$. This only applies to silicon, however. In our case, due to the large number of surface states, the Fermi level is pinned at the semiconductor, resulting in barrier heights that are relatively independent of ϕ_{m}, and for III–V compounds, such as GaAs, is $\phi_{\text{B}} \approx \frac{2}{3}E_{\text{g}} \approx 0.8\text{eV}$.[52]

The fact that I_{dark} in Figure 3 is comparable for the MXene and Au-based devices, and that it is independent of the cathode–anode distance, validates the point that our Ti_3C_2-based electrodes act like any other metal on GaAs. It is thus not surprising that it can substitute for Au, with the advantage of being formed at room temperature, using tabletop equipment, with no need for vacuum deposition, at low cost, while also being transparent to light.

The MX–S–MX device is thus similar to an MSMs and consists of two back-to-back Schottky diodes, with a barrier between MXene and semiconductor, the value of which is primarily determined by the pinned Fermi level on the GaAs side. This contact produces a built-in voltage, a strong local electric field on the GaAs side, and a concomitant depletion region, the width of which depends on the built-in voltage. Application of a bias voltage, causes one of the contacts to become a reverse biased cathode, which dominates current transport.

Figure 1h shows a sketch of the energy band diagram (EBD) of the MX–S–MX device under moderate applied external bias, most of which is dropped at the cathode, extending its depletion region (W_1) to point x_1, with the remainder dropping at the anode and reducing its depletion width (W_2) to point x_2. While W_1 and W_2 are under strong (>10 kV cm^{-1}) e-fields, the remainder of the distance between contacts, namely, ($x_2 - x_1$), is undepleted bulk with no e-field, and is in the so-called below "reach-through" condition. Further increase of bias depletes the whole distance (W), between contacts and is called "flat-band" as shown in Figure 1i.

Figure 1h,i helps elucidate device behavior when light illuminates the gap between the contacts. Several current components can be observed, including the holes that are generated within W_1 and are swept quickly to the cathode. The electrons, on the other hand, drift to the edge of the depletion region, where they would diffuse through the bulk, overcome the built-in voltage at the anode, and are collected there. The electron–hole pairs (EHP) generated in the anode region W_2, have an opposite flux, however, their numbers are much smaller since $W_1 \gg W_2$.

Table 2. Figures of merit (FOM) at ≈300 μW input power, under 8 V bias.

Photodetector	λ [nm]	Figures of merit				
		R [mA W^{-1}]	η [%]	D^* [Jones]	NEP $\left[\frac{\text{W}}{\sqrt{\text{Hz}}}\right]$	DR [dB]
MX–S–MX	532	155	36	8×10^{10}	6.3×10^{-14}	96.7
	780	195	31	8.1×10^{10}	6.1×10^{-14}	96.9
	830	278	42	11.6×10^{10}	4.3×10^{-14}	98.4
Ti/Au MSM	532	95	22	7.9×10^{10}	6.2×10^{-14}	96.8
	780	82	13	7.2×10^{10}	6.9×10^{-14}	96.3
	830	72	11	6.3×10^{10}	7.9×10^{-14}	95.7

Printed by [Drexel University Drexel Unive - 144.118.077.011 - /doi/epdf/10.1002/adma.201903271] at [28/05/2020].

© 2019 WILEY-VCH Verlag GmbH & Co. KGaA, Weinheim

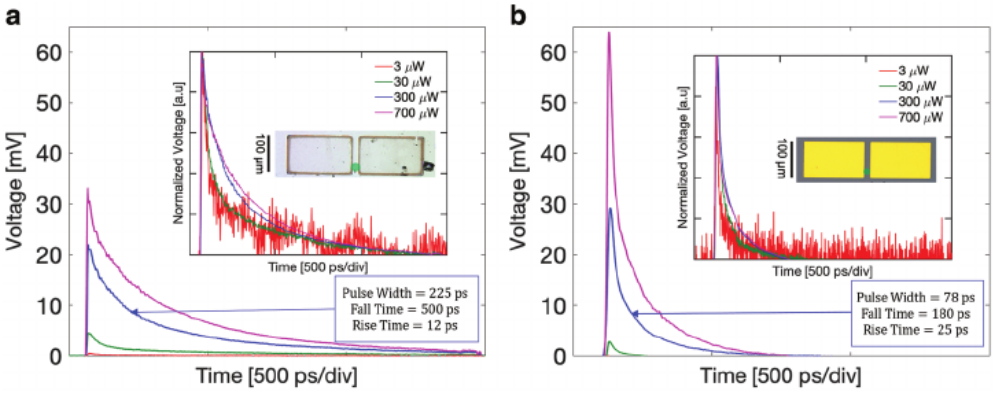

Figure 5. Comparison of the temporal response of MXene- and Ti/Au-based devices to excitation by 100 fs pulses of 830 nm light at 8 V bias under various indicated optical powers. a) MXene device pulse response; inset shows same data normalized to peak amplitude. b) Same as (a) for Ti/Au MSM. Pulse width, rise time, and fall times are indicated for 300 μW optical power. Results for other optical powers are reported in Section S5 in the Supporting Information.

By neglecting carriers recombination, and applying the condition of continuity of current in both depletion regions, the total current of the photodetector is calculated, as detailed in Section S6[11] (Equation (S12)) in the Supporting Information.

The first term in Equation (S12) in the Supporting Information is the most significant and is due to the EHPs that are generated in the cathode and anode depletion regions. The middle two terms are due to carriers generated in the bulk and extracted at the end of the cathode depletion region. The last term is the current that is due to the extraction of the holes at the anode. For the special case here that the undepleted region is much wider than the diffusion length, and $W_1 \gg W_2$, Equation (S12) in the Supporting Information reduces to

$$J = qG(W_1 + L_p) \tag{2}$$

which means that EHPs generated within W_1, and those within a hole diffusion length of it, constitute the majority of the photocurrent. Hence, while contact separation W varies from 5 to 15 to 35 μm, as shown in Section S3 (Figure S1) in the Supporting Information, the cathode depletion width W_1 remains unchanged and depends only on applied bias. As a result, the photocurrents are comparable for these devices, depending only on the applied bias. In the other extreme, the flat-band condition shown in Figure 1i is reached if W is small, and the photocurrent simply saturates at $J = qGW$.

Examining the temporal response, holes generated within W_1 are swept quickly by the electric field and collected at the cathode, while electrons generated within the same region need to traverse the whole gap. Under constant illumination, both carriers are collected in MXene-based devices and, added to the fact that contacts are transparent, result in higher responsivity. In transient response, however, Ti/Au has a stronger built-in field in a larger W_1 which is presumably why they show faster speeds and more efficient carrier collection. It is acknowledged that these considerations based on the analysis outlined above are only qualitative and need further study to elucidate the reasons for the very high responsivity, and comparable speed, of the MXene-based devices. Also, operating beyond reach-through is an optimized condition for device design since it eliminates slow diffusion processes, and is possible to achieve with small feature sizes our fabrication technique allows.

Herein, we show that using a cheap and simple three-step process based on photolithography, spin-coating, and lift-off, transparent MXene contacts with feature sizes limited by lithography can be produced. The resulting contacts are Schottky, which resulted in MXene–GaAs–MXene photodetector devices that outperformed in terms of responsivity, quantum efficiency and dynamic range similar Ti/Au–GaAs–Ti/Au devices. They were also comparable in speed of response, and, at a pulse width of a fraction of a nanosecond, could operate in a few gigahertzs range, meeting stringent requirements of optical detection for tele/data communications. All these performance measures can be improved by device optimization which our fabrication process affords. Due to the scalability of this process, microfabrication of devices can be done for photonic integrated circuit and silicon photonics technologies. Additionally, as Schottky contact, MXene is a strong candidate for use as (transparent) gate of metal–semiconductor field effect transistors (MESFETs), and high electron mobility transistors (HEMTs) which are the dominant devices in high-speed high-power applications.

Finally, MXenes, including $Ti_3C_2T_z$ used here, have the unique attribute that their work function[30] can be adjusted from 2.14 to 5.65 eV by different means, such as hole injection or surface termination using oxygen, fluorine,[53–55] or chlorine.[19] This provides a wider range compared to all metals used in MSM detectors.[56] Consequently, if the Fermi level is not pinned in the semiconductor, as is the case in silicon, MXenes could be used as ohmic, or Schottky contacts at will, resulting in a range of optoelectronic applications, such as having low noise MSMs with Schottky contacts, or high gain photoconductors with two ohmic contacts. Furthermore, the idea that ohmic contacts can be formed by proper surface termination of MXene, is quite appealing to the microelectronic industry.

It should also be mentioned that stability and durability of MXenes remain as important challenges. One promising recent remedy to MXene oxidation in aqueous colloidal suspensions when stored in water at ambient conditions is to simply cap the edges of individual MXene flakes by polyanions such as polyphosphates, polysilicates, and polyborates. This selective functionalization of the edges differently from the surfaces has been shown to significantly reduce their propensity for oxidation even in aerated water for weeks.[57]

Printed by [Drexel University Drexel Unive - 144.118.077.011 - /doi/epdf/10.1002/adma.201903271] at [28/05/2020].

© 2019 WILEY-VCH Verlag GmbH & Co. KGaA, Weinheim

Experimental Section

MXene film preparation is detailed in Section S1 in the Supporting Information.

Photolithography and device fabrication is detailed in Section S2 in the Supporting Information.

Current–voltage (*I–V*) relations were measured at wavelengths of 532, 780, and 830 nm as a function of bias. The biasing voltage was swept from ±8 V, in order to detect for any hysteresis effects. The incident light power was varied from dark to 3, 43, 220, and 700 μW, and then back to dark for all experiments. The photodetector response measurements used a 532 nm continuous wave laser and a 780 and 830 nm mode-locked laser operating at a repetition rate of 76 MHz. In all cases, the laser spot was focused with a 20× microscope objective onto the sample and subsequently expanded to the gap between electrodes. Electrical contact with the pads was made using 60+GHz microwave probes (Picoprobe model 67 A). The bias voltage and current measurements were made through a bias-T using a source meter (Keithley 2400).

Supporting Information

Supporting Information is available from the Wiley Online Library or from the author.

Acknowledgements

B.N. and P.D. acknowledge supports by Singh Center for Nanotechnology at University of Pennsylvania, NSF ICORPS (Award 1904171), and Nanograss Solar LLC. M.C. acknowledges funding from the Office of Naval Research, and M.B. acknowledges NSF Ceramics Division (Award DMR 1740795). This research used resources of the Center for Functional Nanomaterials, which is a U.S.DOE office of Science Facility, at Brookhaven National Laboratory under Contract No. DESC0012704. B.N. conceived the idea, K.M. and L.V. developed and carried out film preparation and device processing, M.C. performed the measurements, P.D. proposed the device fabrication method, and M.B. and B.N. supervised the work. All authors wrote and commented on the manuscript.

Conflict of Interest

The authors declare no conflict of interest.

Keywords

metal–semiconductor–metal, MXene, photodetectors, Schottky contacts, semiconductors, work-function

Received: May 22, 2019
Revised: August 15, 2019
Published online: September 15, 2019

[1] C. Burrus, J. Bowers, R. Tucker, *Electron. Lett.* **1985**, *21*, 262.
[2] C. Lenox, H. Nie, P. Yuan, G. Kinsey, A. Homles, B. Streetman, J. Campbell, *IEEE Photonics Technol. Lett.* **1999**, *11*, 1162.
[3] T. Sugeta, T. Urisu, S. Sakata, Y. Mizushima, *Jpn. J. Appl. Phys.* **1980**, *19*, 459.
[4] S. Assefa, F. Xia, S. W. Bedell, Y. Zhang, T. Topuria, P. M. Rice, Y. A. Vlasov, *Opt. Express* **2010**, *18*, 4986.
[5] F. Koppens, T. Mueller, P. Avouris, A. Ferrari, M. Vitiello, M. Polini, *Nat. Nanotechnol.* **2014**, *9*, 780.
[6] C. H. Liu, Y. C. Chang, T. B. Norris, Z. Zhong, *Nat. Nanotechnol.* **2014**, *9*, 273.
[7] T. Mueller, F. Xia, P. Avouris, *Nat. Photonics* **2010**, *4*, 297.
[8] P. Tassin, T. Koschny, M. Kafesaki, C. M. Soukoulis, *Nat. Photonics* **2012**, *6*, 259.
[9] G. B. Tait, B. Nabet, *IEEE Trans. Electron Devices* **2003**, *50*, 2573.
[10] J. Song, M. Lim, S. S. Lee, B. J. Lee, *Phys. Rev. Appl.* **2019**, *11*, 044040.
[11] L. C. Liou, B. Nabet, *Appl. Opt.* **1996**, *35*, 15.
[12] A. Anwar, B. Nabet, in *1999 SBMO/IEEE MTT-S Int. Microwave and Optoelectronics Conf.*, IEEE, Piscataway, NJ, USA **1999**, pp. 581–584.
[13] B. Nabet, M. Currie, P. Dianat, F. Quaranta, A. Cola, *ACS Photonics* **2014**, *1*, 560.
[14] R. J. Shiue, Y. Gao, Y. Wang, C. Peng, A. D. Robertson, D. K. Efetov, S. Assefa, F. H. Koppens, J. Hone, D. Englund, *Nano Lett.* **2015**, *15*, 7288.
[15] B. Nabet, *Photodetectors: Materials, Devices and Applications in Communications and Imaging Technologies*, Elsevier Science & Technology, Oxford, UK **2015**.
[16] M. Naguib, M. Kurtoglu, V. Presser, J. Lu, J. Niu, M. Heon, L. Hultman, Y. Gogotsi, M. W. Barsoum, *Adv. Mater.* **2011**, *23*, 4248.
[17] M. Sokol, V. Natu, S. Kota, M. W. Barsoum, *Trends Chem.* **2019**, *1*, 210.
[18] J. Halim, K. M. Cook, M. Naguib, P. Eklund, Y. Gogotsi, J. Rosen, M. W. Barsoum, *Appl. Surf. Sci.* **2016**, *362*, 406.
[19] M. Li, J. Lu, K. Luo, Y. Li, K. Chang, K. Chen, J. Zhou, J. Rosen, L. Hultman, P. Eklund, *J. Am. Chem. Soc.* **2019**, *141*, 4730.
[20] M. Naguib, V. N. Mochalin, M. W. Barsoum, Y. Gogotsi, *Adv. Mater.* **2014**, *26*, 992.
[21] M. Khazaei, A. Ranjbar, M. Arai, T. Sasaki, S. Yunoki, *J. Mater. Chem. C* **2017**, *5*, 2488.
[22] B. Anasori, M. R. Lukatskaya, Y. Gogotsi, *Nat. Rev. Mater.* **2017**, *2*, 16098.
[23] J. Pang, R. G. Mendes, A. Bachmatiuk, L. Zhao, H. Q. Ta, T. Gemming, H. Liu, Z. Liu, M. H. Rummeli, *Chem. Soc. Rev.* **2019**, *48*, 72.
[24] K. Hantanasirisakul, Y. Gogotsi, *Adv. Mater.* **2018**, *30*, 1804779.
[25] L. Verger, C. Xu, V. Natu, H. M. Cheng, W. Ren, M. W. Barsoum, *Curr. Opin. Solid State Mater. Sci.* **2019**, *23*, 149.
[26] B. Dyatkin, E. Mamontov, K. M. Cook, Y. Gogotsi, *Prog. Nat. Sci.: Mater. Int.* **2015**, *25*, 631.
[27] A. S. Levitt, M. Alhabeb, C. B. Hatter, A. Sarycheva, G. Dion, Y. Gogotsi, *J. Mater. Chem. A* **2019**, *7*, 269.
[28] N. Kurra, B. Ahmed, Y. Gogotsi, H. N. Alshareef, *Adv. Energy Mater.* **2016**, *6*, 1601372.
[29] Y. Jhon, M. Seo, Y. Jhon, *Nanoscale* **2018**, *10*, 69.
[30] Y. Liu, H. Xiao, W. A. Goddard III, *J. Am. Chem. Soc.* **2016**, *138*, 15853.
[31] P. Zhao, H. Jin, X. Lv, B. Huang, Y. Ma, Y. Dai, *Phys. Chem. Chem. Phys.* **2018**, *20*, 16551.
[32] A. Sarycheva, A. Polemi, Y. Liu, K. Dandekar, B. Anasori, Y. Gogotsi, *Sci. Adv.* **2018**, *4*, eaau0920.
[33] S. Bae, H. Kim, Y. Lee, X. Xu, J. S. Park, Y. Zheng, J. Balakrishnan, T. Lei, H. R. Kim, Y. I. Song, *Nat. Nanotechnol.* **2010**, *5*, 574.
[34] X. Wang, L. Zhi, K. Müllen, *Nano Lett.* **2008**, *8*, 323.
[35] J. Wu, M. Agrawal, H. A. Becerril, Z. Bao, Z. Liu, Y. Chen, P. Peumans, *ACS Nano* **2009**, *4*, 43.
[36] G. Ying, A. D. Dillon, A. T. Fafarman, M. W. Barsoum, *Mater. Res. Lett.* **2017**, *5*, 391.
[37] J. Halim, M. R. Lukatskaya, K. M. Cook, J. Lu, C. R. Smith, L.-Å. Näslund, S. J. May, L. Hultman, Y. Gogotsi, P. Eklund, *Chem. Mater.* **2014**, *26*, 2374.
[38] A. D. Dillon, M. J. Ghidiu, A. L. Krick, J. Griggs, S. J. May, Y. Gogotsi, M. W. Barsoum, A. T. Fafarman, *Adv. Funct. Mater.* **2016**, *26*, 4162.

Printed by [Drexel University Drexel Unive - 144.118.077.011 - /doi/epdf/10.1002/adma.201903271] at [28/05/2020].

 © 2019 WILEY-VCH Verlag GmbH & Co. KGaA, Weinheim

[39] H. Hu, T. Hua, *J. Mater. Chem. A* **2017**, *5*, 19639.
[40] B. Xu, M. Zhu, W. Zhang, X. Zhen, Z. Pei, Q. Xue, C. Zhi, P. Shi, *Adv. Mater.* **2016**, *28*, 3333.
[41] W. Zheng, T. Xie, Y. Zhou, Y. Chen, W. Jiang, S. Zhao, J. Wu, Y. Jing, Y. Wu, G. Chen, *Nat. Commun.* **2015**, *6*, 6972.
[42] S. Binari, M. Marchywka, D. Koolbeck, H. Dietrich, D. Moses, *Diamond Relat. Mater.* **1993**, *2*, 1020.
[43] C. V. Poulton, A. Yaacobi, D. B. Cole, M. J. Byrd, M. Raval, D. Vermeulen, M. R. Watts, *Opt. Lett.* **2017**, *42*, 4091.
[44] R. Pasqualotto, P. Nielsen, *Rev. Sci. Instrum.* **2003**, *74*, 1671.
[45] X. Gong, M. Tong, Y. Xia, W. Cai, J. S. Moon, Y. Cao, G. Yu, C. L. Shieh, B. Nilsson, A. J. Heeger, *Science* **2009**, *325*, 1665.
[46] G. Konstantatos, *Nat. Commun.* **2018**, *9*, 5266.
[47] N. Driscoll, A. G. Richardson, K. Maleski, B. Anasori, O. Adewole, P. Lelyukh, L. Escobedo, D. K. Cullen, T. H. Lucas, Y. Gogotsi, *ACS Nano* **2018**, *12*, 10419.
[48] M. Thunemann, Y. Lu, X. Liu, K. Kılıç, M. Desjardins, M. Vandenberghe, S. Sadegh, P. A. Saisan, Q. Cheng, K. L. Weldy, *Nat. Commun.* **2018**, *9*, 2035.
[49] W. Deng, H. Huang, H. Jin, W. Li, X. Chu, D. Xiong, W. Yan, F. Chun, M. Xie, C. Luo, *Adv. Opt. Mater.* **2019**, *7*, 1801521.
[50] A. Cowley, S. Sze, *J. Appl. Phys.* **1965**, *36*, 3212.
[51] G. B. Tait, B. Nabet, *IEEE Trans. Electron Devices* **2003**, *50*, 2573.
[52] S. M. Sze, K. K. Ng, *Physics of Semiconductor Devices*, John Wiley & Sons, New York **2006**.
[53] M. Khazaei, M. Arai, T. Sasaki, A. Ranjbar, Y. Liang, S. Yunoki, *Phys. Rev. B* **2015**, *92*, 075411.
[54] T. Schultz, N. C. Frey, K. Hantanasirisakul, S. Park, S. J. May, V. B. Shenoy, Y. Gogotsi, N. Koch, *Chem. Mater.* **2019**, *31*, 6590.
[55] J. L. Hart, K. Hantanasirisakul, A. C. Lang, B. Anasori, D. Pinto, Y. Pivak, J. T. van Omme, S. J. May, Y. Gogotsi, M. L. Taheri, *Nat. Commun.* **2019**, *10*, 522.
[56] Z. Kang, Y. Ma, X. Tan, M. Zhu, Z. Zheng, N. Liu, L. Li, Z. Zou, X. Jiang, T. Zhai, *Adv. Electron. Mater.* **2017**, *3*, 1700165.
[57] V. Natu, J. L. Hart, M. Sokol, H. Chiang, M. L. Taheri, M. W. Barsoum, *Angew. Chem., Int. Ed.* **2019**, *58*, 12655.

Printed by [Drexel University Drexel Unive - 144.118.077.011 - /doi/epdf/10.1002/adma.201903271] at [28/05/2020].

 © 2019 WILEY-VCH Verlag GmbH & Co. KGaA, Weinheim